Comparison Between NdFeB and SmCo Permanent Magnets Regarding Eddy Currents in Bearingless PM Synchronous Machines

Daniel Dietz and Andreas Binder

Institute for Electrical Energy Conversion, Technical University of Darmstadt, Germany
ddietz@ew.tu-darmstadt.de

Abstract

PM synchronous machines, used as high-speed drives, typically employ SmCo magnets instead of NdFeB due to the possibly high rotor temperature and the low air gap flux density. SmCo magnets exhibit a lower remanence and a higher electric conductivity than NdFeB material, leading to higher eddy current losses. Additionally, in bearingless PM machines, the asynchronously rotating suspension winding air gap field wave induces eddy currents in the rotor. These lead to a damping and deflection of the air gap field and, thus, to a disturbing rotor force, which may be crucial for the rotor position control.

We discuss the occurrence of the eddy current-originated disturbing force, present as an force error angle, for three PM materials: $SmCo_5$, Sm_2Co_{17} and NdFeB. By measurements on two geometrically identical rotors in a prototype machine, employing a Sm_2Co_{17}- and a NdFeB-PM in the rotor, we show that the force error angle is considerably bigger for the Sm_2Co_{17}-rotor. Still, for the considered small machine dimensions the error angle is small enough to not endanger the rotor position control stability.

1 Introduction

For high-speed machines, the permanent magnet (PM) material is not restricted to NdFeB material such as for highly utilized drives, since for the iron loss reduction low air gap flux

Table 1: Electromagnetic PM material properties (if not designated: data from [1, 2])

		$SmCo_5$	Sm_2Co_{17}	NdFeB
Remanence flux density B_{rem} / T	20 °C	0.85 ... 1.01	0.97 ... 1.12	1.09 ... 1.41
	100 °C	0.823 ... 0.98	0.947 ... 1.09	0.99 ... 1.28
	used[2]	0.947	0.947	1.096
Temperature coefficient[3] $\alpha_{th,rem}$ / $\% \cdot K^{-1}$		−0.04	−0.03	−0.114
Relative permeability $\mu_{r,PM}$		1.025 ... 1.07	1 ... 1.22	0.98 ... 1.145
	used[2]	1.056	1.056	1.068
Electric conductivity κ_{PM} / $MS \cdot m^{-1}$	20 °C	1.67 ... 2[1]	1.18 ... 1.33[1]	0.63 ... 0.71[1]
	used[2]	1.8	1.25	0.8

[1]) According to IEC Standard 60404-8-1[3]; [2]) used value for the analysis; [3]) regarding the remanence flux density at B_{rem} = 20 C°
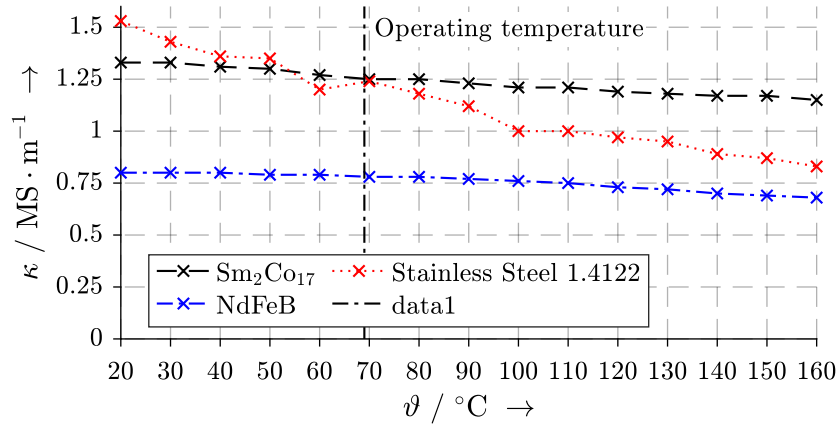
Figure 1: Measured electric conductivity of different PM materials and the shaft material for varying temperature

density values (typically $B < 0.6$ T) are employed. Thus, $SmCo_5$ and Sm_2Co_{17} are feasible alternatives. Also for bearingless motors (BM), which are currently in the focus of research [4], SmCo PMs are used. Prototypes of this topology are realized with high speed and high power values up to 100000 min^{-1} [5] and 60 kW [6]. Subsequently the term B is defined to be the air gap flux density in the radial middle of the mechanical air gap.

The electromagnetic property, such as the remanence flux density B_{rem} and the electric conductivity κ_{PM}, vary much, depending on the manufacturer and the chemical composition. Table 1
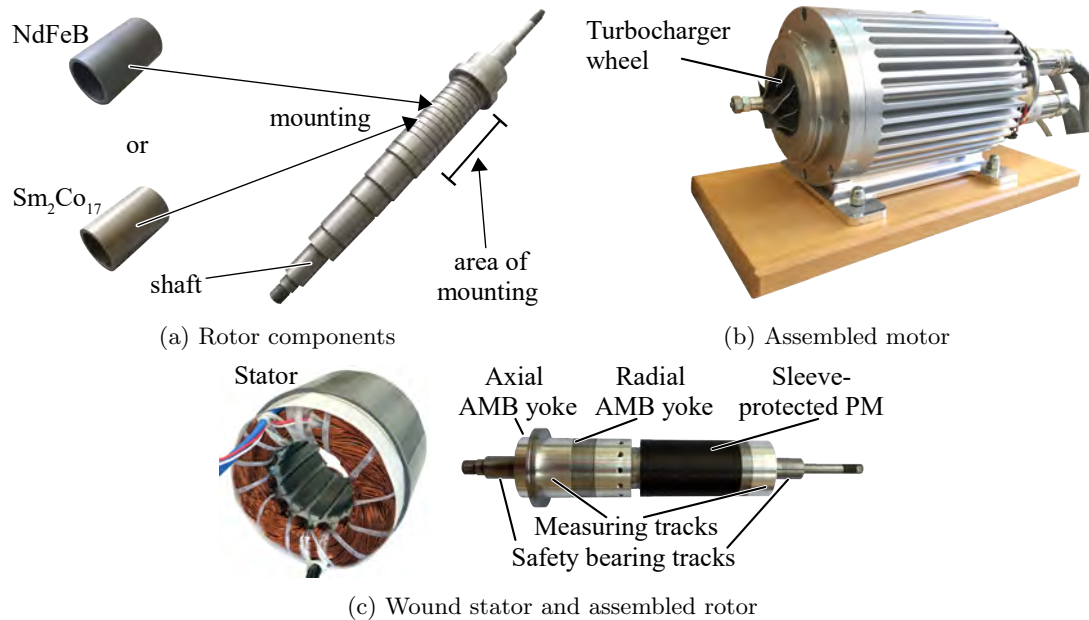

(a) Rotor components

(b) Assembled motor

(c) Wound stator and assembled rotor

Figure 2: Built 1 kW / 60000 min^{-1} bearingless PM synchronous machine

Table 2: Prototype machine properties ($P_\mathrm{N} = 1$ kW, $n_\mathrm{N} = 60000$ min^{-1})

Pole count $2p$ / Suspension winding pole count $2p_\mathrm{L}$	2 / 4
Rated suspension force F_L (equal to gravitational force F_G) / N	5.3
Axial active length l_Fe / mm	40
Stator outer radius $r_\mathrm{s,o}$ / stator inner radius $r_\mathrm{s,i}$ / mm	37.5 / 17.5
Shaft radius r_sh / outer PM radius r_PM / mm	12.25 / 15
PM height h_PM / mm	2.75
Bandage height + mechanical air gap width: δ / mm	2.5
Shaft material: Stainless steel 1.4122, $\mu_\mathrm{r,sh} = 100$	
PM material: two rotors, one with NdFeB and one with Sm$_2$Co$_{17}$ (Table 1)	

shows this variety together with the used values for the analysis. The used remanence flux density B_rem is taken from the comparison between back-EMF measurements and 2D finite element simulations. The used conductivity values are taken from the measurement with demagnetized probes in Fig. 1, based on [7, 8].

In [2] a detailed analysis of a PM conductivity measurement is presented, showing the temperature dependence and anisotropy of the conductivity in and perpendicular to the magnetization direction (1). It reveals that the anisotropy has bigger impact on the conductivity ($\pm 20\%$) than the temperature variation ($\pm 5\%$) up to 150 °C. Unfortunately, it is not possible to model the anisotropy by 2-dimensional analytical or finite element simulations, since the decoupling of the vector potential components is not possible. However, eddy currents are mainly present in axial direction, so the electric conductivity perpendicular to the magnetization direction was measured and is used for the analysis.

The electric conductivity κ_PM determines the penetration depth $d_\mathrm{E,PM}$ and thereby the eddy current distribution in the PM. High-speed machines and also the 1 kW / 60000 min^{-1} prototype machine (Fig. 2, Table 2) employ a solid PM ring for mechanical reasons, so that the eddy current loops are not intersected. Apart from the influence on the eddy current losses, the air gap field distortion by rotor eddy currents in BM leads to a suspension force error angle $\epsilon_\mathrm{err,Ft}$ and to a reduction of the suspension force amplitude $G_\mathrm{Ft,a,0}$. We discuss the occurrence of the disturbing force for different PM materials by calculation in Section 3 and by measurement in Section 4.

2 Air Gap Field Deformation by Eddy Currents

For the generation of a standstill, radial suspension force vector, acting on the rotor in a bearingless PM machine, e.g. to counteract the gravitational force, four air gap field waves (1)–(4) are necessary. The field waves are given in the stator reference frame with the circumference angle γ_m. The suspension winding is required to have a pole count of $2p_\mathrm{L} = 2p \pm 2$ poles, where $2p$ is the rotor pole count. (1) and (3) are the radial and tangential components of the suspension winding air gap field fundamental B_L. The suspension winding is fed by a three-phase current system with synchronous frequency $f_\mathrm{s} = n \cdot p$, where n is the rotational speed. Thus, the suspension winding fundamental synchronous velocity is $v_\mathrm{s,L} = 2\tau_\mathrm{p,L} \cdot f_\mathrm{s}$, where $\tau_\mathrm{p,L}$ is the suspension winding pole pitch.

(2) and (4) are the radial and tangential components of the rotor air gap field fundamental B_R with $2p$ poles. Its synchronous velocity is $v_{s,R} = 2\tau_p \cdot f_s \neq v_{s,L}$, where τ_p is the rotor pole pitch. v_s is different from $v_{s,L}$ due to $2p_L = 2p \pm 2$.

$$B_{L,r}(r, \gamma_m, t) = \mathrm{Re}\left\{\underline{B}_{L,r}(r) \cdot e^{j \cdot p_L \gamma_m} \cdot e^{-j \cdot (p \cdot 2\pi \cdot n \cdot t + \varphi_L)}\right\} \tag{1}$$
$$= \left|\underline{B}_{L,r}(r)\right| \cdot \cos(p_L \gamma_m - p \cdot 2\pi \cdot n \cdot t - \varphi_L - \Delta\gamma_{Ft,r})$$

$$B_{R,r}(r, \gamma_m, t) = \mathrm{Re}\left\{\underline{B}_{R,r}(r) \cdot e^{j \cdot p\gamma_m} \cdot e^{-j \cdot (p \cdot 2\pi \cdot n \cdot t + \varphi_R)}\right\} \tag{2}$$
$$= \hat{B}_{R,r}(r) \cdot \cos(p\gamma_m - p \cdot 2\pi \cdot n \cdot t - \varphi_R)$$

$$B_{L,\gamma}(r, \gamma_m, t) = \mathrm{Re}\left\{\underline{B}_{L,\gamma}(r) \cdot e^{j \cdot p_L \gamma_m} \cdot e^{-j \cdot \left(p \cdot 2\pi \cdot n \cdot t + \varphi_L + \frac{\pi}{2}\right)}\right\} \tag{3}$$
$$= \left|\underline{B}_{L,\gamma}(r)\right| \cdot \sin(p_L \gamma_m - p \cdot 2\pi \cdot n \cdot t - \varphi_L - \Delta\gamma_{Ft,\gamma})$$

$$B_{R,\gamma}(r, \gamma_m, t) = \mathrm{Re}\left\{\underline{B}_{R,\gamma}(r) \cdot e^{j \cdot p\gamma_m} \cdot e^{-j \cdot \left(p \cdot 2\pi \cdot n \cdot t + \varphi_R + \frac{\pi}{2}\right)}\right\} \tag{4}$$
$$= \hat{B}_{R,p\gamma}(r) \cdot \sin(p\gamma_m - p \cdot 2\pi \cdot n \cdot t - \varphi_R)$$

Due to the different synchronous velocity $v_s \neq v_{s,L}$, the asynchronously rotating suspension winding fundamental induces eddy currents in the rotor parts. The resulting suspension winding fundamental amplitude is damped and phase-shifted due to the eddy current reaction field. The damping of the field wave amplitudes is included in the absolute value $|\underline{B}|$ of the complex phasor $\underline{B} = |\underline{B}| \cdot e^{j \cdot \Delta\gamma_{Ft}}$. The phase-shifting of the asynchronous field waves is considered by the angle $\Delta\gamma_{Ft}$ of the complex phasor.

For the analytical magnetic field calculation, including rotor eddy currents, the formulation in rotor-fixed coordinates is needed. The circumference angle in rotor-fixed coordinates is $\gamma_R = \gamma_m - 2\pi \cdot n \cdot t$. The suspension air gap fundamental components in rotor-fixed coordinates are given in (5), (6).

$$B_{L,r}(r, \gamma_R, t) = \mathrm{Re}\left\{\underline{B}_{L,r}(r) \cdot e^{j \cdot p_L \gamma_R} \cdot e^{-j \cdot \left[\underbrace{(p - p_L) \cdot n}_{f_R} \cdot 2\pi \cdot t + \varphi_L\right]}\right\} \tag{5}$$

$$B_{L,\gamma}(r, \gamma_R, t) = \mathrm{Re}\left\{\underline{B}_{L,\gamma}(r) \cdot e^{j \cdot p_L \gamma_R} \cdot e^{-j \cdot \left[\underbrace{(p - p_L) \cdot n}_{f_R} \cdot 2\pi \cdot t + \varphi_L - \frac{\pi}{2}\right]}\right\} \tag{6}$$

(5), (6) contain the rotor frequency f_R, which is equal to the slip frequency. For the fundamental suspension winding air gap field wave, the rotor frequency is given in (7). It shows that f_R only depends on the rotor speed n for a standstill suspension force vector. Eddy currents are induced due to $f_R = |-n|$ for topologies with $p_L = p + 1$.

$$f_R = (p - p_L) \cdot n = f_s - n \cdot (p \pm 1) = \begin{cases} -n & \text{for } p_L = p + 1 \\ n & \text{for } p_L = p - 1 \end{cases} \tag{7}$$

The rotor and suspension winding fundamental of a bearingless machine can be calculated 2-dimensionally (2D), either analytical [9, 10, 11] or by simulations based on the finite element method (FEM). The analytical calculation is based on a slotless model of concentric regions, whereas the FEM model includes the real, slotted, geometry. The calculation of the field waves is not in the scope of this paper. It was addressed in [12].
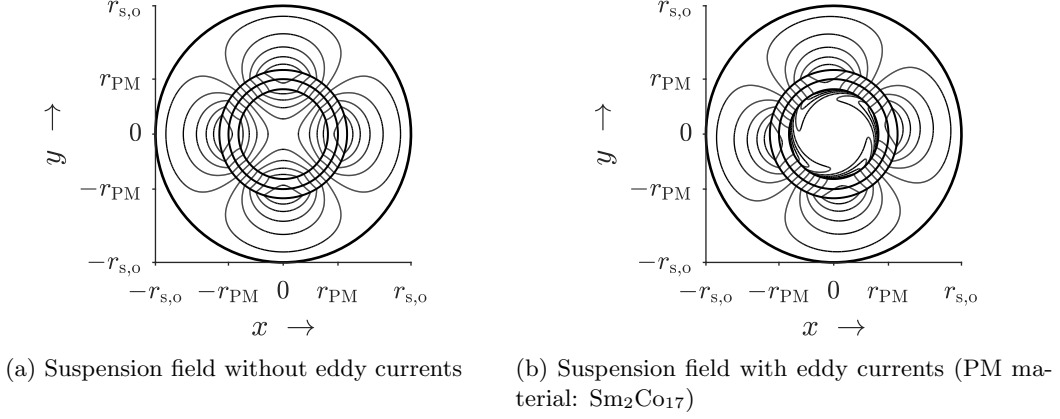
(a) Suspension field without eddy currents

(b) Suspension field with eddy currents (PM material: Sm_2Co_{17})

Figure 3: Analytically calculated magnetic field lines of the suspension winding field for the prototype (Table 2) at $n = 60000$ min^{-1}, $\left|\vec{F}_{\mathrm{L}}\right| = 5.3$ N $= \left|\vec{F}_{\mathrm{G}}\right|$

(a) Sm_2Co_{17}, $2p_{\mathrm{L}} = 4$
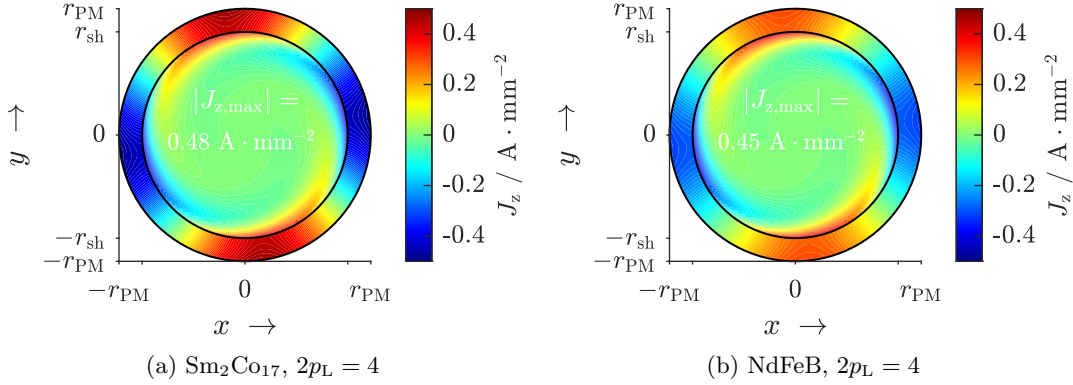
(b) NdFeB, $2p_{\mathrm{L}} = 4$

Figure 4: Analytically calculated current density J_{z} in the rotor parts of the prototype machine (Table 2) due to suspension field fundamental at $n = 60000$ min^{-1}, $\left|\vec{F}_{\mathrm{L}}\right| = 5.3$ N $= \left|\vec{F}_{\mathrm{G}}\right|$

Results are given here for the prototype machine (Fig. 2, Table 2). Fig. 3a (3b) shows the analytically calculated field lines of the suspension winding fundamental without (with) rotor eddy currents at rated speed $n = 60000$ min^{-1} in case of Sm_2Co_{17} PM material. The eddy currents prevent the suspension winding field from entering the rotor shaft due to the small penetration depth of the shaft material ($d_{\mathrm{E,sh}} < 0.3$ mm). Also they lead to a deflection of the air gap field (shift angle $\Delta\gamma_{\mathrm{Ft}}$). The eddy current density in z-direction in the rotor parts is given in Fig. 4. The higher conductive Sm_2Co_{17}-material (Fig. 4a) leads to larger eddy current amplitudes in the permanent magnet than the NdFeB-material (Fig. 4b).

Table 3 gives a comparison of the fundamental air gap flux density components for the prototype machine, which are determined by 2D FEM simulation (*JMAG Designer 19.1*) and by the analytical calculation [12]. Since the iron parts of the prototype machine are not magnetically saturated, only the slot opening effect leads to deviations between analytical calculation and simulation, because it is not considered in the analytical calculation. The radial field quantities by analytical calculation overestimate the simulated solution.

Table 3: Comparison between analytically calculated and simulated air gap fundamental field wave amplitudes in the middle of the mechanical air gap (2D) for the prototype machine (Table 2) at $n = 60000$ min^{-1}, $F_L = 5.3$ N $= F_G$

	Without eddy currents		With eddy currents	
	Simulation	Analytical	Simulation	Analytical
$\hat{B}_{R,r}$ / mT	440.28	443.86 (+0.81%)	440.28	443.86 (+0.81%)
$\hat{B}_{R,\gamma}$ / mT	12.26	11.73 (-4.31 %)	12.26	11.73 (-4.31 %)
$\hat{B}_{L,r}$ / mT	8.48	8.80 (+4.53 %)	7.92	8.10 (+2.22 %)
$\hat{B}_{L,\gamma}$ / mT	4.98	5.03 (+0.95%)	5.02	5.08 (+1.12%)
$\Delta\gamma_{Ft,r}$	0	0	12.21°	12.88° (+5.54 %)
$\Delta\gamma_{Ft,\gamma}$	0	0	$-1.08°$	$-1.06°$ (+1.85 %)
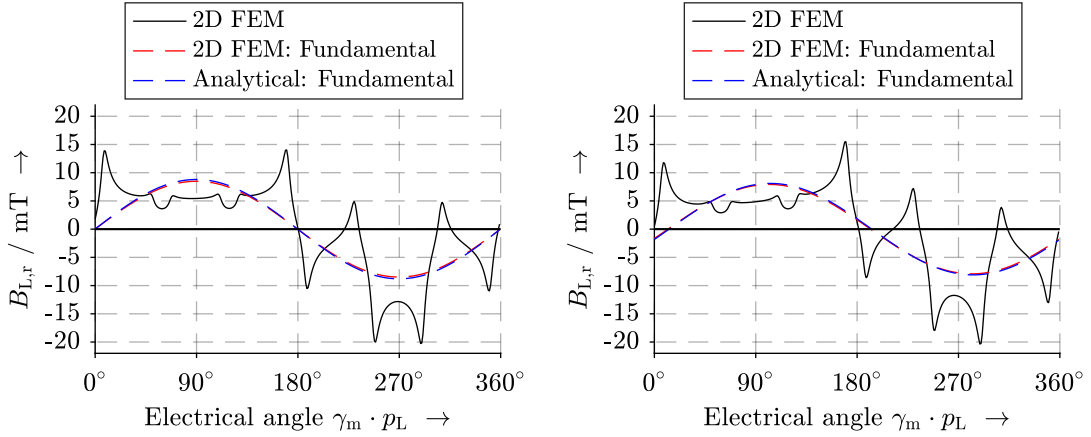
(a) Suspension winding radial air gap field without eddy currents

(b) Suspension winding radial air gap field with eddy currents ($\Delta\gamma_{Ft,r} \approx 12.5°$, Sm$_2Co_{17}$)

Figure 5: Comparison between analytically calculated and simulated air gap flux density radial component for the prototype machine (Table 2) at $n = 60000$ min^{-1} in the middle of the mechanical air gap

There are many elaborate options to include the slot opening effect via permeance functions, such as [13, 14, 15]. The deviation between the analytical calculation and the simulation is $< 6\%$. Also the air gap field deformation by rotor eddy currents is well represented by the analytical calculation, so that the slot opening effect is generally neglected for the analytical calculations. Fig. 5 compares the spatial distribution of the radial air gap field waves to the determined field fundamentals from Table 3. By comparing Fig. 5a and 5b the effect of the rotor eddy currents becomes clearly visible as damping and shifting of the radial suspension field fundamental.

3   Eddy Current Influence on the Suspension Force

Due to the assumed material linearity for the analytical calculation, the overall radial and tangential field components B_r and B_γ are given by the superposition of the stator and rotor field waves. For the suspension force calculation, the 2-dimensional *Maxwell* stress tensor, including B_r and B_γ, in cylindrical coordinates (9) is integrated over a closed surface in the air gap at radius $r_{cal} = r_{s,i} - \delta/2$ (8). The forces are expressed in stator-fixed coordinates. Since we only consider a standstill force vector, the time-dependency is omitted here for clarity.

$$\begin{pmatrix} F_x \\ F_y \end{pmatrix} = \int\limits_{0}^{l_{Fe}} \int\limits_{0}^{2\pi} \begin{pmatrix} f_r(\gamma_m) \cdot \cos(\gamma_m) - f_\gamma(\gamma_m) \cdot \sin(\gamma_m) \\ f_r(\gamma_m) \cdot \sin(\gamma_m) + f_\gamma(\gamma_m) \cdot \cos(\gamma_m) \end{pmatrix} \cdot \mathrm{d}\gamma_m \mathrm{d}z \qquad (8)$$

$$\begin{pmatrix} f_r(\gamma_m) \\ f_\gamma(\gamma_m) \end{pmatrix} \bigg|_{r=r_{cal}} = \frac{1}{2 \cdot \mu_0} \cdot \begin{pmatrix} B_r^2(r_{cal}, \gamma_m) - B_\gamma^2(r_{cal}, \gamma_m) \\ 2 \cdot B_r(r_{cal}, \gamma_m) \cdot B_\gamma(r_{cal}, \gamma_m) \end{pmatrix} \qquad (9)$$

Inserting the radial and tangential components of the rotor and the suspension winding air gap field waves, satisfying $p_L = p + 1$, from (3),(4) and (1),(2) into (8),(9) yields the expression for the standstill radial suspension force vector $\vec{F}_L = F_x \cdot \vec{e}_x + F_y \cdot \vec{e}_y$ (10), (11). The tangential component of the rotor air gap field is here neglected for clarity, since its contribution to the suspension force is $< 1\%$.

$$F_x = \frac{\pi \cdot r_{cal} \cdot l_{Fe}}{2 \cdot \mu_0} \cdot \hat{B}_{R,r}(r_{cal}) \cdot \left[\left| \underline{B}_{L,r}(r_{cal}) \right| \cdot \sin(\varphi_R - \varphi_L - \Delta\varphi_{Ft,r}) + \qquad (10) \right.$$

$$\left. \left| \underline{B}_{L,\gamma}(r_{cal}) \right| \cdot \sin(\varphi_R - \varphi_L - \Delta\varphi_{Ft,\gamma}) \right]$$

$$F_y = \frac{\pi \cdot r_{cal} \cdot l_{Fe}}{2 \cdot \mu_0} \cdot \hat{B}_{R,r}(r_{cal}) \cdot \left[\left| \underline{B}_{L,r}(r_{cal}) \right| \cdot \cos(\varphi_R - \varphi_L - \Delta\varphi_{Ft,r}) + \qquad (11) \right.$$

$$\left. \left| \underline{B}_{L,\gamma}(r_{cal}) \right| \cdot \cos(\varphi_R - \varphi_L - \Delta\varphi_{Ft,\gamma}) \right]$$

If no rotor eddy currents are present, (10), (11) can be simplified to (12), here only shown for the x-direction. In (12), $\varphi_{F,ref}$ is the angle, which determines the direction of the suspension force, e.g. $\varphi_{F,ref} = 0$ for $\vec{F}_L = F_y \cdot \vec{e}_y$.

$$F_x = \frac{\pi \cdot r_{cal} \cdot l_{Fe}}{2 \cdot \mu_0} \cdot \hat{B}_{R,r}(r_{cal}) \cdot \left[\hat{B}_{L,r}(r_{cal}) + \hat{B}_{L,\gamma}(r_{cal}) \right] \cdot \sin\left(\underbrace{\varphi_R - \varphi_L}_{\varphi_{F,ref}} \right) \qquad (12)$$

According to (10), (11), the bearing force amplitude $\left| \vec{F}_L \right|$ is decreased ($\left| \vec{F}_L \right| < \left| \vec{F}_{L,ref} \right|$) by eddy currents, due to $\left| \underline{B}_{L,r} \right| < \hat{B}_{L,r}$ and the spatial alignment φ_F of the bearing force vector is different from the set-point bearing force vector ($\varphi_{F,ref} \neq \varphi_F$), due to $\Delta\gamma_{Ft,r} \neq 0$, $\Delta\gamma_{Ft,\gamma} \neq 0$. The occurring spatial error angle $\epsilon_{err,Ft}$ (Fig. 6) of a standstill suspension force vector $\vec{F}_{L,ref} = F_{y,ref} \cdot \vec{e}_y$ is given in (13), whereas (14) shows the decrease of the bearing force vector by the ratio $G_{Ft,a,0} = F_y / F_{y,ref}$. With a 2D analytical calculation ($2D_{an}$), with a 2D FEM simulation ($2D_{FEM}$) or with a 3D FEM simulation ($3D_{FEM}$), the resulting forces F_x and F_y are inserted into (13), (14) for the calculation of the rotor forces, accounting for the eddy
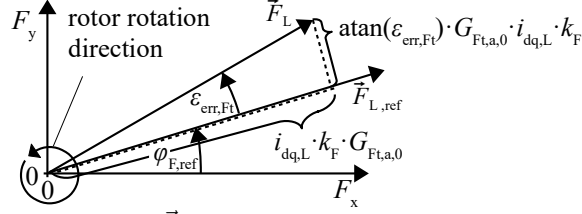
Figure 6: Suspension force vector ($\vec{F}_\mathrm{L}$) deflection by $G_{\mathrm{Ft,a,0}}$ and $\epsilon_{\mathrm{err,Ft}}$ due to the eddy current effect ($i_{\mathrm{dq,L}}$: suspension current, k_F: force-current coefficient without eddy currents)

current effect.

$$\epsilon_{\mathrm{err,Ft}} = \mathrm{atan}\left(\frac{F_\mathrm{x}}{F_\mathrm{y}}\right) = \mathrm{atan}\left(\frac{\left|\underline{B}_{\mathrm{L},p_\mathrm{L},p,\mathrm{r}}\right| \cdot \sin(\Delta\gamma_{\mathrm{Ft,r}}) + \left|\underline{B}_{\mathrm{L},\gamma}\right| \cdot \sin(\Delta\gamma_{\mathrm{Ft},\gamma})}{\left|\underline{B}_{\mathrm{L,r}}\right| \cdot \cos(\Delta\gamma_{\mathrm{Ft,r}}) + \left|\underline{B}_{\mathrm{L},\gamma}\right| \cdot \cos(\Delta\gamma_{\mathrm{Ft},\gamma})}\right) \tag{13}$$

$$G_{\mathrm{Ft,a,0}} = \frac{F_\mathrm{y}}{F_{\mathrm{y,ref}}} = \frac{\mathrm{Re}\left\{\underline{B}_{\mathrm{L,r}}\left(r_{\mathrm{cal}}\right) + \underline{B}_{\mathrm{L},\gamma}\left(r_{\mathrm{cal}}\right)\right\}}{\hat{B}_{\mathrm{L,r}}\left(r_{\mathrm{cal}}\right) + \hat{B}_{\mathrm{L},\gamma}\left(r_{\mathrm{cal}}\right)} \tag{14}$$

Fig. 7a shows that the suspension force amplitude decrease $G_{\mathrm{Ft,a,0}}$ (14) decreases for rising PM electric conductivity κ_{PM}. Also the force error angle $\epsilon_{\mathrm{err,Ft}}$ in Fig. 7b increases almost linear with rising PM electric conductivity κ_{PM} due to the resistance limitation of the eddy currents ($d_{\mathrm{E,PM}} \approx 12\mathrm{mm} \gg h_{\mathrm{PM}} = 2.75$ mm). Thus, for non-segmented PM, NdFeB leads to the smallest suspension force degradation. The results are summarized in Table 4. Consequently, also the rotor eddy current losses $P_{\mathrm{d,Ft,R}}$ are the smallest for the NdFeB material (Fig. 8). The big deviation between analytical calculation and FEM simulation is due to the neglect of the slot opening effect in the analytical model. It shows that the asynchronously rotating field waves due to the modulation of the rotor field by the slot openings account for approximately half of the total eddy current losses.
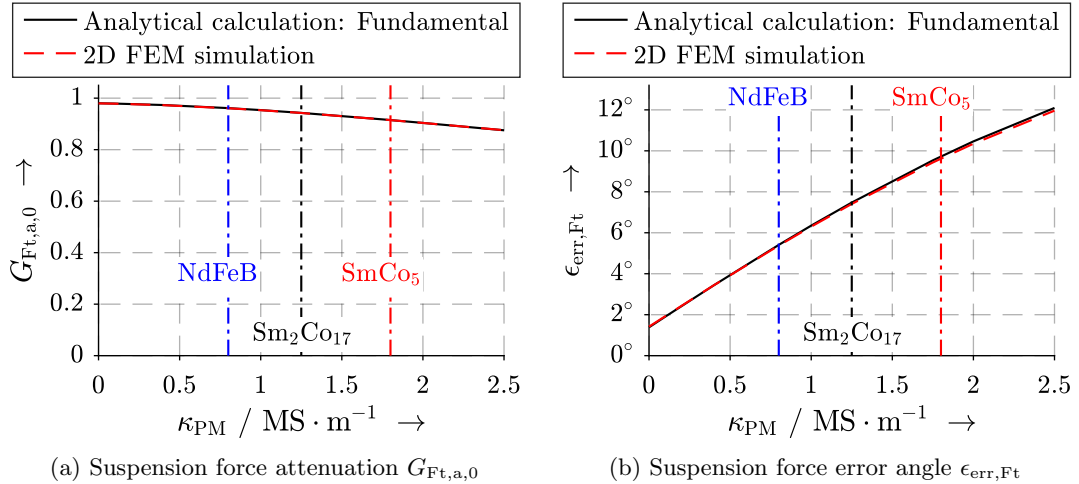

(a) Suspension force attenuation $G_{\mathrm{Ft,a,0}}$

(b) Suspension force error angle $\epsilon_{\mathrm{err,Ft}}$

Figure 7: Calculated and simulated suspension force amplitude attenuation $G_{\mathrm{Ft,a,0}}$ and error angle $\epsilon_{\mathrm{err,Ft}}$ for a standstill suspension force vector $\vec{F} = F_\mathrm{g} \cdot \vec{e}_\mathrm{y}$, depending on the electric PM conductivity κ_{PM}, used remanence flux density: $B_{\mathrm{rem}} = 1$ T
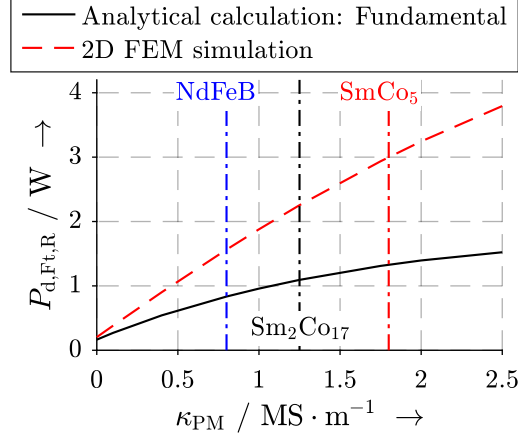
Figure 8: Calculated and simulated rotor eddy current losses $P_{\mathrm{d,Ft,R}} = P_{\mathrm{d,Ft,PM}} + P_{\mathrm{d,Ft,sh}}$ depending on the electric PM conductivity κ_{PM}, used remanence flux density: $B_{\mathrm{rem}} = 1$ T

Table 4: Suspension force attenuation $G_{\mathrm{Ft,a,0}}$, error angle $\epsilon_{\mathrm{err,Ft}}$ and rotor eddy current losses $P_{\mathrm{d,Ft,R}}$ for a SmCo$_5$, a Sm$_2$Co$_{17}$ and a NdFeB PM (prototype data from Table 2)

	SmCo$_5$			Sm$_2$Co$_{17}$			NdFeB		
	$G_{\mathrm{Ft,a,0}}$	$\epsilon_{\mathrm{err,Ft}}$	$P_{\mathrm{d,Ft,R}}$	$G_{\mathrm{Ft,a,0}}$	$\epsilon_{\mathrm{err,Ft}}$	$P_{\mathrm{d,Ft,R}}$	$G_{\mathrm{Ft,a,0}}$	$\epsilon_{\mathrm{err,Ft}}$	$P_{\mathrm{d,Ft,R}}$
2D$_{\mathrm{an}}$	0.91	9.6°	1.3 W	0.94	7.4°	1.1 W	0.96	5.4°	0.8 W
2D$_{\mathrm{FEM}}$	0.92	9.5°	3.0 W	0.94	7.4°	2.3 W	0.96	5.4°	1.6 W

4 Identification of Eddy Current Disturbing Forces by Measurements

In order to identify the eddy current effect by measurement, an accurate determination of the rotor angle $\gamma_{\mathrm{m}} = p \cdot 2\pi \cdot n$ is of high importance. Thus, the time span t_{cal} between current and rotor angle ($\gamma_{\mathrm{m,act}}$) evaluation and PWM output must be compensated in the inverter by a feed-forward of the rotor angle ($\gamma_{\mathrm{m,cor}}$) (15). The compensated rotor angle is $\tilde{\gamma}_{\mathrm{m}}$.

$$\tilde{\gamma}_{\mathrm{m}} = \left(\gamma_{\mathrm{m,act}} + \gamma_{\mathrm{m,cor}}\right), \mathrm{mod}(2\pi) = \left(\gamma_{\mathrm{m,act}} + t_{\mathrm{cal}} \cdot \omega_{\mathrm{s}}\right), \mathrm{mod}(2\pi) \tag{15}$$

For the used inverter with a 150 MHz processor the calculation takes about 2500 cycles leading to $t_{\mathrm{cal}} = 2500/150$ Hz $= 16.7$ ns. At $n = 60000$ min^{-1} this equals 1.7% of the electrical period, leading to an angle deviation of 6° at $n = 60000$ min^{-1}. The rotor is accelerated to half rated speed by speed control. Then the speed control is switched off so that the rotor slows down by no-load losses (zero drive current $i_{\mathrm{q,D}} = 0$). In this situation the voltage drop in d_{D}-axis is zero and not speed dependent if the rotor angle is determined correctly. If this is not the case, t_{cal} has to be adapted in (15).

Additionally, the rotor angle determination for high-speed machines is prone to a non-linear sensor delay over the wide range of speed, here: $n = 0 \ldots 60000$ min^{-1}. Despite the angle correction (15), the rotor angle $\tilde{\gamma}_{\mathrm{m}}$ can differ from the real value γ_{m}. To analyze this error angle $\epsilon_{\mathrm{err,inv}}$, a speed-down test by no-load losses (zero drive current $i_{\mathrm{q,D}} = 0$) is conducted.

The error angle $\epsilon_{\text{err,inv}}$ is calculated by (16). Fig. 9 shows the result for the prototype machine. For the accurate determination of $\epsilon_{\text{err,Ft}}$, the angle $\epsilon_{\text{err,inv}}$ must be considered as an offset (17). The big noise of $\epsilon_{\text{err,inv}}$ in Fig. 9 at very low speed is due to the small voltage drop $u_{\text{q,D}}$ in the q-axis of the drive voltage system.

$$\epsilon_{\text{err,inv}} = \text{atan}\left(\frac{u_{\text{d,D}}|_{i_{\text{q,D}}=i_{\text{d,D}}=0}}{u_{\text{q,D}}|_{i_{\text{q,D}}=i_{\text{d,D}}=0}}\right) \tag{16}$$

$$\gamma_{\text{m}} = \tilde{\gamma}_{\text{m}} - \epsilon_{\text{err,inv}} \tag{17}$$

The suspension currents $i_{\text{d,L}}$ and $i_{\text{q,L}}$ give information about the radial bearing force vector $\vec{F}_{\text{L}}$ which points in opposite direction to the gravitational force $\vec{F}_{\text{G}}$ at stand still ($\vec{F}_{\text{L}} = F_{\text{y}} \cdot \vec{e}_{\text{y}}$). As speed increases, the disturbing orthogonal force $F_{\text{x}} \propto \epsilon_{\text{err,Ft}}$ increases due to the eddy current effect ($f_{\text{R}} = |n|$) and so the orthogonal suspension current $i_{\text{d,L}}$ increases. In order to exclude the disturbing force which is caused by the interference of the drive winding air gap field with the rotor field [16], the rotor is accelerated to rated speed by speed control and slows down by no-load losses with $i_{\text{q,D}} = i_{\text{d,D}} = 0$.

The suspension currents ($i_{\text{d,L}}$, associated to a force in x-direction, $i_{\text{q,L}}$, associated to a force in y-direction) give access to the radial forces on the rotor at rotation. Rotational frequent oscillations are filtered ("force-free rotation" [17]), so that most of the geometrical inaccuracies in the machine do not influence the position controller output. Only DC effects, such as eddy current effect on a standstill bearing force vector, are visible. The tuning of the rotor initial angle is carefully done in a way that for an oscillation of the reference signal in y-position no variation in x-position occurs. Together with the aforementioned speed-dependent correction of the rotor angle γ_{m}, the error angle $\epsilon_{\text{err,Ft}}$ is determined via (18) and the force amplitude reduction $G_{\text{Ft,a,0}}$ via (19).

$$\epsilon_{\text{err,Ft}} \approx \tan\left(\frac{i_{\text{d,L,act}}}{i_{\text{q,L,act}}}\right) - \epsilon_{\text{err,inv}} \tag{18}$$

$$G_{\text{Ft,a,0}} \approx \frac{i_{\text{q,L,act}}(n=0)}{i'_{\text{q,L}}} = \frac{\frac{i_{\text{q,L,act}}(n=0)}{\cos(\epsilon_{\text{err,inv}})}}{\frac{i_{\text{q,L,act}}}{\cos(\epsilon_{\text{err,inv}})} + \tan(\epsilon_{\text{err,Ft}}) \cdot i_{\text{d,L,act}}} \tag{19}$$

For the calculation of $\epsilon_{\text{err,Ft}}$ (18), the measured currents $i_{\text{d,L,act}}$ and $i_{\text{q,L,act}}$ are directly used. The calculation of $G_{\text{Ft,a,0}}$, requires the measured current $i_{\text{q,L,act}}(n=0)$ at zero speed and the

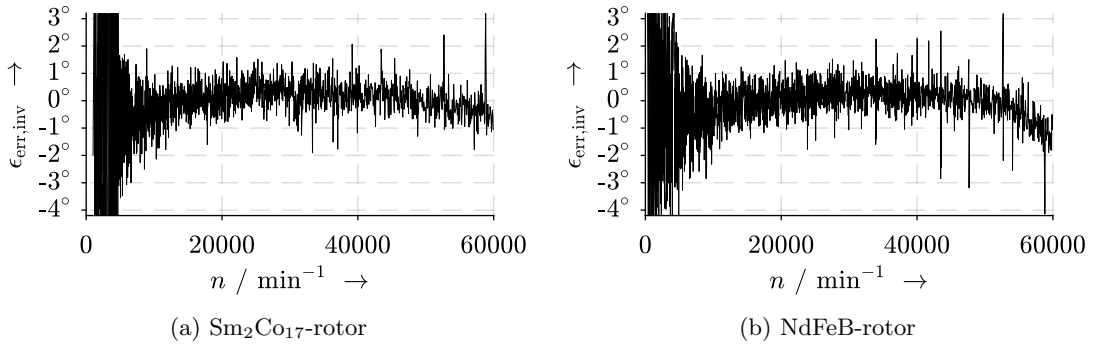

(a) $\text{Sm}_2\text{Co}_{17}$-rotor

(b) NdFeB-rotor

Figure 9: Measured error angle $\epsilon_{\text{err,inv}}$ (16) due to rotor angle sensor delay at varying speed n
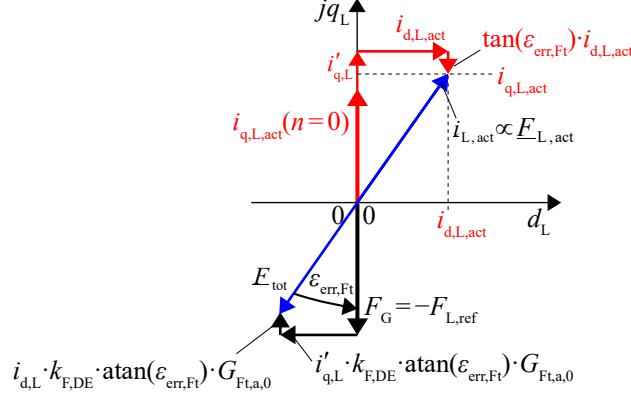
Figure 10: Schematic suspension current vector and rotor force vector equilibrium (correct rotor angle determination provided)

current $i'_{q,L}$ (Fig. 10). Fig. 10 shows schematically how the suspension current vectors and the rotor force vectors are composed in the stator-fixed coordinate frame.

The results for the prototype machine are shown in Fig. 11. Table 5 summarizes the eddy current related disturbing force angle $\epsilon_{err,Ft}$ and bearing force attenuation $G_{Ft,a,0}$ in the prototype machine at rated speed $n_N = 60000 \ \mathrm{min}^{-1}$ for both analyzed PM materials: Sm_2Co_{17} and NdFeB.

Generally, the NdFeB-rotor exhibits a 34% smaller force error angle (measured value) due to the electric conductivity κ_{PM}, which is 35% smaller for the NdFeB than for Sm_2Co_{17} (Table 1). The proportionality $\kappa_{PM} \propto \epsilon_{err,Ft}$ holds for resistance-limited eddy currents. The 2D calculation and simulation results agree well but overestimate the error angle by 72% due to the neglected axial end effect. Even for slender rotors, the end effects are considerable, since the suspension winding pole pitch $\tau_{p,L}$ (here: $\tau_{p,L} = 27.5$ mm) may be in the range of the axial length l_{Fe} (here: $l_{Fe} = 40$ mm). Even the 3-dimensional FEM simulation overestimates the error angle by 22%. This deviation may be due to material degradation at the PM surface during the mounting of the bandage or by slightly orthotropic conductivity properties [2], which could not be identified in the simple conductivity measurement (Fig. 1). The amplitude attenuation of the 3-dimensional simulations agree well with the measured results. Following the results from Fig. 11, the speed dependency of $G_{Ft,a,0}$ and $\epsilon_{err,Ft}$ can be considered approximately linear

Table 5: Comparison of different determination techniques for the eddy current disturbing forces in the prototype machine (Table 2) at $n_N = 60000 \ \mathrm{min}^{-1}$

	Sm_2Co_{17}		NdFeB	
	$G_{Ft,a,0}$	$\epsilon_{err,Ft}$	$G_{Ft,a,0}$	$\epsilon_{err,Ft}$
2D$_{an}$	0.951	7.09°	0.970	5.06°
2D$_{FEM}$	0.958	6.63°	0.975	4.63°
3D$_{FEM}$	0.968	5.06°	0.987	3.47°
Measurement	0.969	4.13°	0.982	2.73°

(a) Force amplitude attenuation $G_{\mathrm{Ft,a,0}}$: Sm_2Co_{17}-rotor

(b) Force amplitude attenuation $G_{\mathrm{Ft,a,0}}$: NdFeB-rotor

(c) Force error angle $\epsilon_{\mathrm{err,Ft}}$: Sm_2Co_{17}-rotor

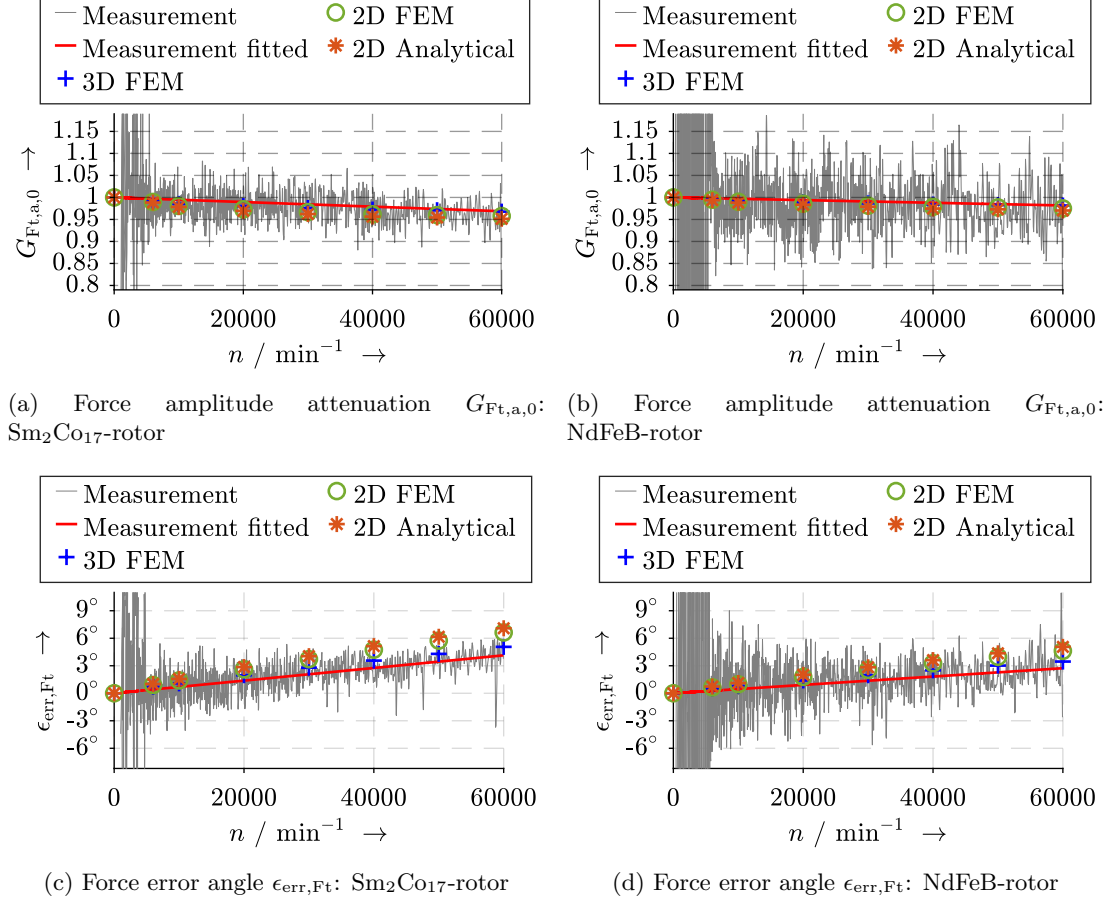(d) Force error angle $\epsilon_{\mathrm{err,Ft}}$: NdFeB-rotor

Figure 11: Comparison of different determination techniques for the force amplitude attenuation $G_{\mathrm{Ft,a,0}}$ and the force error angle $\epsilon_{\mathrm{err,Ft}}$ at the prototype machine (Table 2) for varying speed n

(20), (21). Since the speed is equal to the slip frequency $f_{\mathrm{R}} = |n|$ (7), this holds as long as the eddy currents are resistance-limited.

$$G_{\mathrm{Ft,a,0}}\left(n\right) \approx 1 - \frac{n}{n_{\mathrm{N}}} \cdot \left[1 - G_{\mathrm{Ft,a,0}}\left(n = n_{\mathrm{N}}\right)\right] \tag{20}$$

$$\epsilon_{\mathrm{err,Ft}}\left(n\right) \approx \frac{n}{n_{\mathrm{N}}} \cdot \epsilon_{\mathrm{err,Ft}}\left(n = n_{\mathrm{N}}\right) \tag{21}$$

The measured suspension force attenuation $G_{\mathrm{Ft,a,0}} > 0.95$ and error angle $\epsilon_{\mathrm{err,Ft}} < 5°$ are not crucial for the rotor position control in the considered prototype machine. However, eddy current originated disturbance forces may be much bigger for larger machine dimensions, since the suspension winding fundamental intrudes deeper into the conductive rotor parts. Also for higher speed values n and, thus, higher slip frequency values f_{R}, the eddy current effect increases. Thus, especially for larger and faster rotating machines either low conductive PM material, such as NdFeB, or a segmentation is required to keep the eddy current effect small.

5   Conclusion

The influence of the PM material in bearingless machines on the suspension force degradation is discussed. The attenuation and phase-shifting of the suspension force due to rotor eddy currents is shown by calculation, simulation and measurements on a 1 kW / 60000 min^{-1} prototype machine. Low conductive PM material, such as NdFeB, leads to a smaller disturbing force by eddy currents. In the considered prototype machine even higher conductive PM materials, such as Sm_2Co_{17}, lead to a very small eddy current effect. However, for larger machines or at higher speed values the eddy current originated disturbance forces increase and may not be neglected anymore.

6   Acknowledgments

References

[1] {Vacuumschmelze GmbH & Co. KG}, "Rare Earth Permanent Magnets Vacodym Vacomax," 2014. [Online]. Available: https://vacuumschmelze.de/shared/quickNav/Downloads

[2] S. Ruoho, M. Haavisto, E. Takala, T. Santa-Nokki, and M. Paju, "Temperature Dependence of Resistivity of Sintered Rare-Earth Permanent-Magnet Materials," *IEEE Transactions on Magnetics*, vol. 46, no. 1, pp. 15–20, Jan. 2010, http://ieeexplore.ieee.org/document/5357499/.

[3] "Specifications of Individual Materials - Magnetically Hard Materials," in *IEC Standard 60404-8-1*, 2004, p. 65.

[4] H.-D. Stölting, E. Kallenbach, and W. Amrhein, Eds., *Handbook of fractional-horsepower drives*. Berlin, Heidelberg, New York: Springer-Verlag, 2008.

[5] Y. Fu, M. Takemoto, S. Ogasawara, and K. Orikawa, "Investigation of Operational Characteristics and Efficiency Enhancement of an Ultra-High-Speed Bearingless Motor at 100,000 r/min," *IEEE Transactions on Industry Applications*, vol. 56, no. 4, pp. 3571–3583, Apr. 2020.

[6] Z. Liu, A. Chiba, Y. Irino, and Y. Nakazawa, "Optimum Pole Number Combination of a Buried Permanent Magnet Bearingless Motor and Test Results at an Output of 60 kW With a Speed of 37000 r/min," *IEEE Open Journal of Industry Applications*, vol. 1, pp. 33–41, Feb. 2020.

[7] F. M. Smits, "Measurement of Sheet Resistivities with the Four-Point Probe," *The Bell System Technical Journal*, vol. 57, no. 3, pp. 711–718, 1958.

[8] O. Gutfleisch, M. Verdier, I. Harris, and A. Ray, "Characterisation of rare earth-transition metal alloys with resistivity measurements," *IEEE Transactions on Magnetics*, vol. 29, no. 6, pp. 2872–2874, Nov. 1993, http://ieeexplore.ieee.org/document/281081/.

[9] Z. Q. Zhu, D. Howe, E. Bolte, and B. Ackermann, "Instantaneous magnetic field distribution in brushless permanent magnet DC motors. I. Open-circuit field," *IEEE Transactions on Magnetics*, vol. 29, no. 1, pp. 124–135, Jan. 1993.

[10] A. Rahideh and T. Korakianitis, "Analytical magnetic field distribution of slotless brushless permanent magnet motors – Part I. Armature reaction field, inductance and rotor eddy current loss calculations," *IET Electric Power Applications*, vol. 6, no. 9, p. 628, 2012.

[11] M. Markovic and Y. Perriard, "Analytical Solution for Rotor Eddy-Current Losses in a Slotless Permanent-Magnet Motor: The Case of Current Sheet Excitation," *IEEE Transactions on Magnetics*, vol. 44, no. 3, pp. 386–393, Mar. 2008.

[12] D. Dietz and A. Binder, "Eddy Current Influence on the Control Behavior of Bearingless PM
     Synchronous Machines," *IEEE Transactions on Industry Applications*, vol. 57, no. 6, 2021, to be
     published.

[13] F. W. Carter, "The Magnetic Field of the Dynamo-electric Machine," *Journal of the Institution
     of Electrical Engineers*, vol. 64, no. 359, pp. 1115 – 1138, Nov. 1926.

[14] J. R. Anglada, S. M. Suleiman, and A. Qazalbash, "Influence of curvature on air-gap magnetic field
     distribution and rotor losses in PM electric machines," *COMPEL - The international journal for
     computation and mathematics in electrical and electronic engineering*, vol. 36, no. 4, pp. 871–891,
     Mar. 2017, http://www.emeraldinsight.com/doi/10.1108/COMPEL-05-2016-0200.

[15] D. Zarko, D. Ban, and T. A. Lipo, "Analytical calculation of magnetic field distribution in the
     slotted air gap of a surface permanent-magnet motor using complex relative air-gap permeance,"
     IEEE Transactions on Magnetics, vol. 42, no. 7, pp. 1828–1837, 2006.

[16] G. Messager and A. Binder, "Derivation of forces and force interferences in a double conical high-
     speed bearingless permanent magnet synchronous motor," in *International Electric Machines and
     Drives Conference (IEMDC)*, Miami, USA, May 2017, pp. 1–8.

[17] G. Schweitzer and E. H. Maslen, Eds., *Magnetic Bearings: Theory, Design, and Application to
     Rotating Machinery*.   Berlin, Dordrecht, Heidelberg, New York: Springer-Verlag, 2009.